Incorporation of Manganese Dioxide within Ultraporous Activated Graphene for High-Performance Electrochemical Capacitors

Xin Zhao,[†,‡] Lili Zhang,[†] Shanthi Murali,[†] Meryl D. Stoller,[†] Qinghua Zhang,[‡] Yanwu Zhu,[§,*] and Rodney S. Ruoff[†,*]

[†]Department of Mechanical Engineering and the Materials Science and Engineering Program, The University of Texas at Austin, One University Station C2200, Austin, Texas 78712, United States, [‡]State Key Laboratory for Modification of Chemical Fibers and Polymer Materials, College of Materials Science and Engineering, Donghua University, Shanghai 201620, People's Republic of China, and [§]Department of Materials Science and Engineering, University of Science and Technology of China, Hefei 230036, People's Republic of China

ABSTRACT

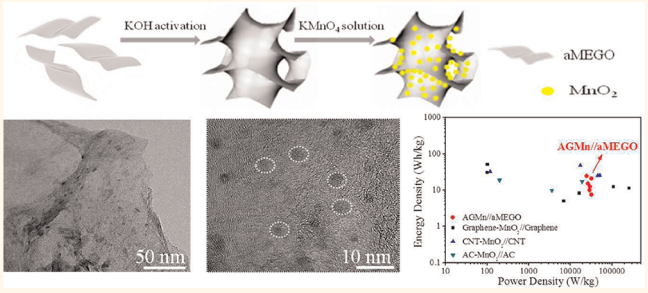

Manganese dioxide (MnO_2) particles 2−3 nm in size were deposited onto a porous "activated microwave expanded graphite oxide" (aMEGO) carbon scaffold *via* a self-controlled redox process. Symmetric electrochemical capacitors were fabricated that yielded a specific capacitance of 256 F/g (volumetric: 640 F/cm^3) and a capacitance retention of 87.7% after 1000 cycles in 1 M H_2SO_4; when normalized to MnO_2, the specific capacitance was 850 F/g. Asymmetric electrochemical capacitors were also fabricated with aMEGO/MnO_2 as the positive electrode and aMEGO as the negative electrode and had a power density of 32.3 kW/kg (for an energy density of 20.8 Wh/kg), an energy density of 24.3 Wh/kg (for a power density of 24.5 kW/kg), and a capacitance retention of 80.5% over 5000 cycles.

KEYWORDS: aMEGO · MnO_2 · composites · asymmetric · electrochemical capacitors

Electrochemical capacitors (ECs), also known as supercapacitors or ultracapacitors, are of practical interest owing to their high power electrical energy storage and exceptionally long cycle life; they currently fill the gap between batteries and conventional electrostatic capacitors.[1] On the basis of the charge storage mechanism, ECs can be categorized as electric double-layer capacitors (EDLCs) and pseudocapacitors. EDLCs store energy by forming a double layer of electrolyte ions on a conductive surface and commonly use high-surface-area carbon-based materials for electrodes.[2−4] Pseudocapacitors depend on the fast and reversible redox reactions at the electrode surface for charge storage; typical active materials include transition-metal oxides such as ruthenium oxide, iron oxide, nickel hydroxide, manganese oxide,[5−9] as well as electrically conductive polymers such as polyanilines, polypyrroles, and polythiophenes.[10−13] To date, lower operating voltages and limited cycle life have prevented widespread commercialization of pseudocapacitors. However, the large specific capacitance of these faradaic electrodes (typically 300−1000 F/g) exceeds that of carbon-based materials with pure EDLC capacitance, resulting in great interest to overcome these limitations.[14]

Manganese dioxide (MnO_2) is a promising pseudocapacitive electrode material for ECs due to its low cost, relatively environmentally benign properties, and high theoretical specific capacitance (~1380 F/g).[15] As such, it is a promising alternative to RuO_2-based acid systems or state-of-the-art commercial carbon-based EDLCs.[16−18] However, its poor electrical conductivity and low mass loading in a planar ultrathin configuration have significantly limited the energy storage capacity of MnO_2.[19−21] One strategy to increase capacity is to deposit a thin MnO_2 layer on support materials that are highly conductive, have a high specific surface area, and are electrochemically stable. For example, a hybrid structure with a several-micrometer-thick crust of MnO_2 deposited on

* Address correspondence to r.ruoff@mail.utexas.edu, zhuyanwu@ustc.edu.cn.

Received for review March 23, 2012 and accepted May 3, 2012.

Published online May 03, 2012
10.1021/nn3012916

carbon nanofoam[22] yielded a specific capacitance of about 110 F/g (for the hybrid nanofoam/MnO_2 material) and a specific capacitance of 170−230 F/g (when normalized to just the MnO_2). Composites with different sizes of MnO_2 nanoparticles embedded into the mesoporous carbon matrix[23] demonstrated specific capacitances of up to 220 F/g with 26 wt % loading of MnO_2 for a specific capacitance of 600 F/g when normalized to MnO_2. More recently, a thin layer (20−30 nm) of MnO_2 was deposited onto a three-dimensional mesoporous structure that consists of chemically modified graphene, showing a high specific capacitance up to 389 F/g.[24] Total capacitance has been improved by depositing MnO_2 in porous carbon materials; however, the specific capacitance normalized to the MnO_2 phase is usually far below the theoretical value of MnO_2 ultrathin films (~1380 F/g),[15] which could be due to the low surface-to-volume ratio of the MnO_2 particles. Because pseudocapacitance depends on surface reactions, MnO_2 particle size plays a crucial role in realizing its full pseudocapacitance. Relatively large pores (and thus a low mass density) in the carbon structures used as scaffolds will also lead to poor volumetric capacitances. Thus, by choosing a carbon support structure with high conductivity, suitable porosity, and high specific surface area, one may expect to not only achieve a high specific gravimetric capacitance but also improve the volumetric capacitance. An example of a system where high values of 500−1250 F/g were reported is that of nanoscale MnO_x particles electrodeposited onto sheets composed of multiwalled carbon nanotubes (CNTs).[25]

In our previous work, a novel porous and highly conductive carbon material was synthesized using potassium hydroxide chemical activation of exfoliated graphite oxide.[26] The activated microwave expanded graphite oxide (aMEGO) has extremely high specific surface areas (up to 3100 m^2/g), a continuous three-dimensional (3D) network of highly curved atom thick walls of carbon, and an ultraporous structure with pore sizes ranging from about 0.6 to 5 nm. With a measured powder electrical conductivity of ~500 S/m and excellent electrochemical stability (a specific capacitance retention of 97% after 10 000 cycles in ionic liquid electrolyte), aMEGO is an attractive scaffold candidate for MnO_2.

Herein, we report the fabrication of aMEGO/MnO_2 (in short, AGMn) composites *via* a simple and cost-effective redox process. The self-controlled reaction between aMEGO and potassium permanganate ($KMnO_4$) under neutral pH conditions led to the formation of a homogeneous deposition of nanoscale MnO_2 particles throughout the ultraporous aMEGO structures. The resultant 3D AGMn composite architecture retained most of the structural properties of the aMEGO, which facilitates easy access of the electrolyte ions into the electrodes. With the AGMn composites as electrodes in ECs, specific gravimetric capacitances of up to 256 F/g were obtained in 1 M H_2SO_4 aqueous solution, corresponding to a volumetric specific capacitance of 640 F/cm^3, with a capacitance retention of 87.7% after 1000 cycles (for the AGMn sample with 38.1 wt % MnO_2). The specific capacitance is 850 F/g when normalized to MnO_2 content (for the AGMn sample with 8.1 wt % MnO_2). Furthermore, asymmetric EC devices with AGMn (for the AGMn sample with 8.1 wt % MnO_2) as the positive electrode and aMEGO as the negative electrode in 1 M Na_2SO_4 electrolyte had a power density of 32.3 kW/kg (at the energy density of 20.8 Wh/kg), an energy density of 24.3 Wh/kg (at the power density of 24.5 kW/kg), and a cycling performance of 80.5% capacitance retention over 5000 cycles. The aMEGO could serve as a scaffold for other transition-metal oxides as well as conducting polymers.

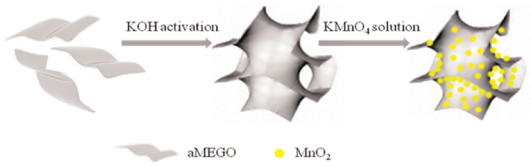

Scheme 1. Schematic illustration showing the self-controlled redox deposition of manganese oxide in aMEGO.

RESULTS AND DISCUSSION

Different amounts of MnO_2 were deposited by soaking aMEGO in $KMnO_4$ aqueous solution with reaction times ranging from 5 to 120 min, leading to samples denoted here as AGMn-*x*min (*x* = 5, 10, 30, 60, 90, 120). The preparation of AGMn nanostructures is illustrated in Scheme 1. Under a neutral pH condition, the reaction between carbon and $KMnO_4$ is as follows:[27]

$$4MnO_4^- + 3C + H_2O \rightarrow 4MnO_2 + CO_3^{2-} + 2HCO_3^-$$

The mass loadings of MnO_2 in the AGMn samples as estimated by thermogravimetric analyses (TGA) were 8.1, 10.2, 15.5, 24.3, 29.9, and 38.1% by weight in the order of increasing reaction times. The MnO_2 loading follows a nearly linear dependence for deposition times longer than 5 min (Figure S1a in Supporting Information). Moreover, the derivative thermogravimetric (DTG) curves (Figure S1b) suggest that the temperature for carbon combustion was lower for higher MnO_2 content, which can be explained by the local modification of carbon species by MnO_2 and the catalytic function of the Mn species as studied in our previous work.[28]

Figure 1 shows the X-ray diffraction (XRD) patterns for the AGMn composites with different reaction times (10 and 120 min), as well as that of aMEGO. For all samples, two diffraction peaks appear at around 23° and 43°, corresponding to the (002) and (101) diffraction peaks of graphitic carbons,[23,29] respectively. The peak intensity (after removing the background) was

lower for the AGMn composites and is mainly attributed to the incorporation of MnO_2 nanoparticles. No obvious MnO_2 diffraction peaks can be observed in the spectra of AGMn compared to that of aMEGO, probably due to the fact that the MnO_2 particles in the samples are of such small size and likely have an amorphous or poorly crystalline structure.[22] There is a slight upward sloping at around 36.8 and 65.7° for AGMn-10min and AGMn-120min, and these two peaks become more obvious after calcination in air at 400 °C for 3 h (AGMn-120min-h) and correspond to the (006) and (119) peaks of birnessite MnO_2 (JCPDF 18-0802), respectively. In addition, the XPS spectrum (Figure S2) for AGMn-10min contains a Mn $2p_{3/2}$ peak at about 641.8 eV and a Mn $2p_{1/2}$ peak at about 653.6 eV, with a spin-energy separation of 11.8 eV, showing that the predominant Mn oxidation state is a valence state of +4.[30] No obvious Mn $2p_{3/2}$ signal of $KMnO_4$ at 647 eV was observed, indicating that the permanganate ions have been reduced to MnO_2.[22]

The SEM images in Figure 2a,b show that the as-prepared AGMn-10min composite retains the 3D structure and porous morphology of aMEGO; the composite looks very similar to the aMEGO as described in our previous report,[26] suggesting that the redox reaction between carbon and $KMnO_4$ did not change the overall morphology of aMEGO. In addition, both the high-resolution SEM image (Figure 2b) and the bright-field scanning transmission electron microscopy (BF-STEM) image (Figure 2c) for the same area show that a homogeneous distribution of MnO_2 nanoparticles has been obtained without any sign of additional MnO_2 formed on the exterior surface of this AGMn-10min sample. The uniform distribution of MnO_2 was also confirmed by energy-dispersive spectroscopy (EDS) elemental mapping. Figure 2d shows a SEM image of the same area combined with EDS mapping images made from K-line energy densities of C, Mn, and O. Compared to the C mapping image, the Mn and O mappings show lower distribution intensity, further indicating that there is little MnO_2 present on the exterior of the carbon. Only for the longest deposition time of 120 min does the formation of MnO_2 nanoflakes on the external structure become noticeable (Figure S3). We surmise that nanoscale amorphous MnO_2 particles are incorporated within the interior of the nanoporous structure of aMEGO, and the porous structure prevents the reaggregation of MnO_2 nanoparticles during the high-temperature calcination process.

The dispersion of MnO_2 nanoparticles in the aMEGO can also be observed with transmission electron microscopy (TEM) imaging. The low-magnification images (Figure 3a,b) show that MnO_2 nanoparticles (indicated by the dotted circles) appear as particles with size of ~2−3 nm with no larger aggregates present. At higher magnification (Figure 3c), highly curved carbon layers with fringes were observed, showing that the porous structure of aMEGO has been preserved after the incorporation of MnO_2. The measured lattice spacing of the MnO_2 particles of ~2.42 Å is close to the value of 2.44 Å of the (006) planes of birnessite[31] and corresponds to the peak at 36.8° in the XRD pattern (Figure 1). No larger aggregates of MnO_2 nanoparticles were found even after the sample was annealed at 400 °C for 3 h (Figure S4), implying that the MnO_2

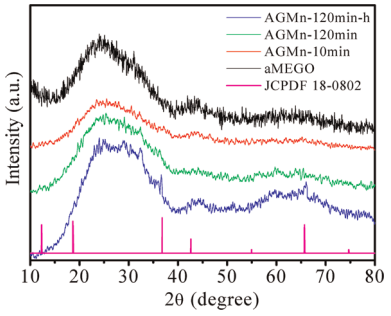

Figure 1. XRD patterns of aMEGO and AGMn-120min and the same sample after being annealed (AGMn-120min-h) as well as the standard pattern of birnessite MnO_2 (JCPDF 18-0802).

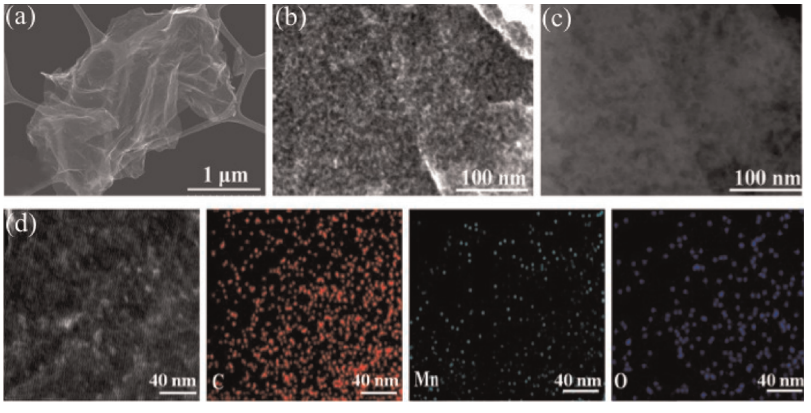

Figure 2. (a) Low-magnification and (b) high-magnification SEM images of the AGMn-10min composite, (c) BF-STEM image of the same area as (b), (d) SEM image combined with EDS mapping in the same area and relative intensities of C (red), Mn (green), and O (blue) elements.

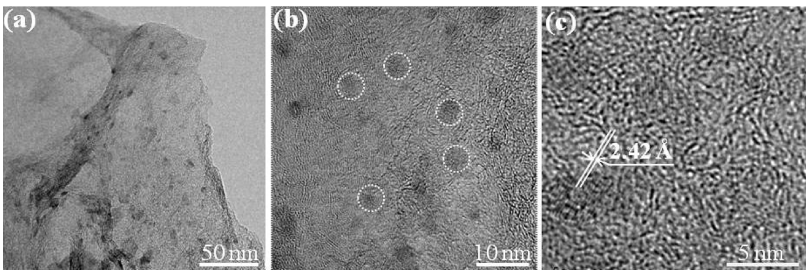

Figure 3. (a,b) Low- and (c) high-magnification transmission electron micrographs of AGMn-10min showing nanoscale MnO_2 particles in aMEGO.

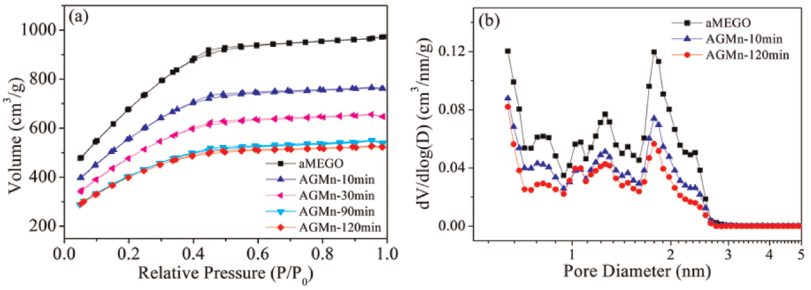

Figure 4. (a) Nitrogen adsorption isotherms of aMEGO and AGMn composites with various reaction times. (b) Pore size distributions of aMEGO and two typical AGMn composites.

TABLE 1. MnO_2 Loadings and Pore Structure Parameters of the aMEGO and AGMn Composites

sample	MnO_2 content (%)	specific surface area (m^2/g)	pore volume (cm^3/g)	pore size (nm)
aMEGO	0	2690	1.44	1.8
AGMn-10min	8.1	2483	1.14	1.8
AGMn-30min	15.5	1998	0.98	1.8
AGMn-90min	29.9	1417	0.82	1.8
AGMn-120min	38.1	1391	0.78	1.8

nanoparticles are homogeneously dispersed within and tightly confined by the porous aMEGO structure.

The porosity of the AGMn composites was studied by nitrogen adsorption, and the adsorption isotherms for aMEGO and for the AGMn composites are shown in Figure 4a. All samples are found to have typical IV isotherm curves indicating a micromesoporous structure.[28] The specific surface area (Table 1) decreases from 2690 m^2/g for aMEGO to 2483 m^2/g for AGMn-10min and to 1391 m^2/g for AGMn-120min, still significantly higher than other reported carbon/MnO_2 composites.[22,28,32,33] The cumulative pore volume decreases from 1.44 cm^3/g for the aMEGO to 1.14 and 0.78 cm^3/g for the samples with 10 and 120 min deposition times, respectively. The decrease in the specific surface area and the total pore volume with increase of the MnO_2 loading is, we think, mainly due to the higher density of the composites rather than the pore-filling of MnO_2, which is confirmed by the unchanged average pore size and the pore size distribution shown in Figure 4b. On the basis of previous reports,[34−36] pore-filling would significantly reduce the pore size, even at a relatively low loading level of guest materials. The negligible change in the pore size and its distribution after the treatment with $KMnO_4$ indicated that the MnO_2 nanoparticles did not occupy or block the space of the pores, but possibly embedded in the pore walls of the aMEGO, as previously reported for mesoporous carbon,[22] thus preserving the continuous 3D architecture of the pristine aMEGO.

To explore the AGMn composites as EC electrodes, the electrochemical properties of our samples were first characterized in symmetric two-electrode ECs with cyclic voltammogram (CV), galvanostatic charge/discharge, and frequency response measurements in a 1 M H_2SO_4 aqueous solution. Figure 5a shows the CV curves for aMEGO and AGMn composites at a scan rate of 20 mV/s. The relatively symmetrical rectangular shape of the CV plots indicates that the samples have an ideal EC behavior; the gravimetric current density increases with MnO_2 deposition time, suggesting that the capacitance is improved by incorporating pseudocapacitive materials into the 3D nanoporous structures. This also can be confirmed from the triangle shape of the charge/discharge curves and an increase of discharge times in Figure 5b. Furthermore, the AGMn-120min composite maintains good performance from both CV curves and charge/discharge plots at increasing scan rates (Figure S5a,b).

The specific capacitance for the AGMn composite electrodes was calculated from the discharge curves (Experimental Section); the specific pseudocapacitance contributed from just the MnO_2 was also

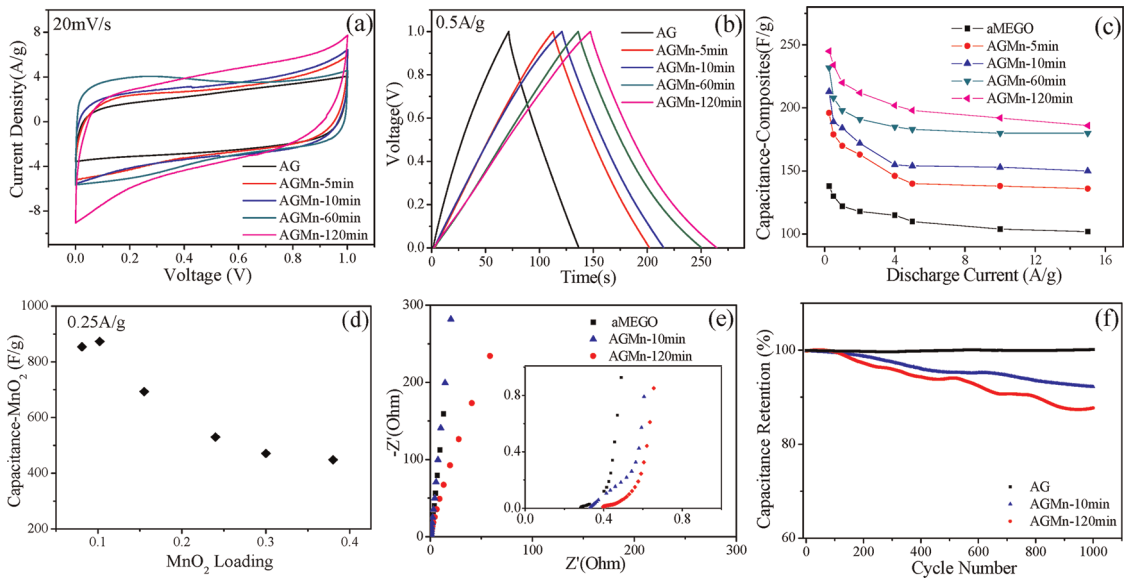

Figure 5. (a) Cyclic voltammograms (at 20 mV/s) and (b) charge/discharge curves (at 0.5 A/g) for bare aMEGO electrode and AGMn composite electrodes with various loadings. (c) Specific capacitances of aMEGO and AGMn composites with various loadings plotted as the function of charge/discharge current densities. (d) Gravimetric capacitances based on MnO_2 as a function of the loadings at a current density of 0.25 A/g. (e) Nyquist curves of aMEGO and AGMn composites. (f) Capacitance retention of symmetric cells based on aMEGO and AGMn electrodes measured in a 1 M H_2SO_4 aqueous electrolyte.

determined. As shown in Figure 5d, specific capacitances normalized to MnO_2 reach 850 F/g at 0.25 A/g for the AGMn-10min sample, much higher than MnO_2 in other carbon/MnO_2 composites and comparable to CNT/MnO_2 composites.[16,37] The high value shows that the homogeneous dispersion of nanoscale MnO_2 particles could reduce the diffusion length of ions within the pseudocapacitive phase, ensuring a greater utilization of the active materials.[38] However, performance begins to decrease for deposition times longer than 10 min, probably due to excess MnO_2 on the outside of the aMEGO, as shown in the SEM image for AGMn-120min (Figure S3). In spite of the excess MnO_2, a total gravimetric specific capacitance of up to 256 F/g for the AGMn-120min sample at a scan rate of 0.25A/g is still achieved for longer deposition times (Figure 5c). As the current density is increased from 0.25 to 20 A/g, this value falls to 187 F/g and then remains approximately constant, still higher than that of other carbon/MnO_2 or conductive polymer hybrid electrodes (80−170 F/g) at the same current density.[39,42,43]

A frequency response analysis (FRA) in the frequency range from 1 MHz to 10 mHz yields the Nyquist plot for aMEGO and AGMn composites, as shown in Figure 5e with an expanded view of the high-frequency region in the inset. All plots feature the most vertical line in a low-frequency region, indicating a nearly ideal capacitive behavior. From the magnified data in the high-frequency range, both AGMn-10min and AGMn-120min composites show very low equivalent series resistance (ESR) values (about 0.34 and 0.4 ohms, respectively) close to that of aMEGO (about 0.28 ohms), suggesting that the AGMn electrodes have very small resistance with good ion response at high-frequency ranges even with a high loading of MnO_2. The small resistances are also confirmed by observing the negligible voltage drops at the beginning of discharge curves in Figure 5b. The very low ESR values indicate that the aMEGO material with its ultrahigh specific surface area can indeed act as a highly conductive substrate for MnO_2 deposition.

Several unique characteristics of the AGMn composites which make them a promising candidate as high-performance EC electrode materials include the following: (i) the unique architecture and extremely high surface areas of aMEGO permit a large loading of MnO_2 particles and also facilitate free access of electrolyte ions to the electrode surfaces; and (ii) the conformal and homogeneous dispersion of nanoscale MnO_2 particles throughout the conductive, ultraporous aMEGO structures reduces the diffusion length of ions within the pseudocapacitive phase ensuring an efficient utilization of the active materials. Furthermore, a capacitance retention of 87.7% was achieved after 1000 cycles for the AGMn-120min sample when scanned at a high current density of 15 A/g (Figure 5f), indicating both good high-rate performance and good stability of the as-prepared AGMn composites.

Asymmetric EC systems that incorporate a different material for each electrode promise a wider operating voltage and thus provide increased energy densities.[43−45] We assembled hybrid ECs using AGMn-10min composites (with 8.1 wt % MnO_2) as the positive electrodes and aMEGO as the negative electrodes in aqueous electrolyte, as shown in Figure 6a. According to a previous investigation of an activated carbon MnO_2/activated

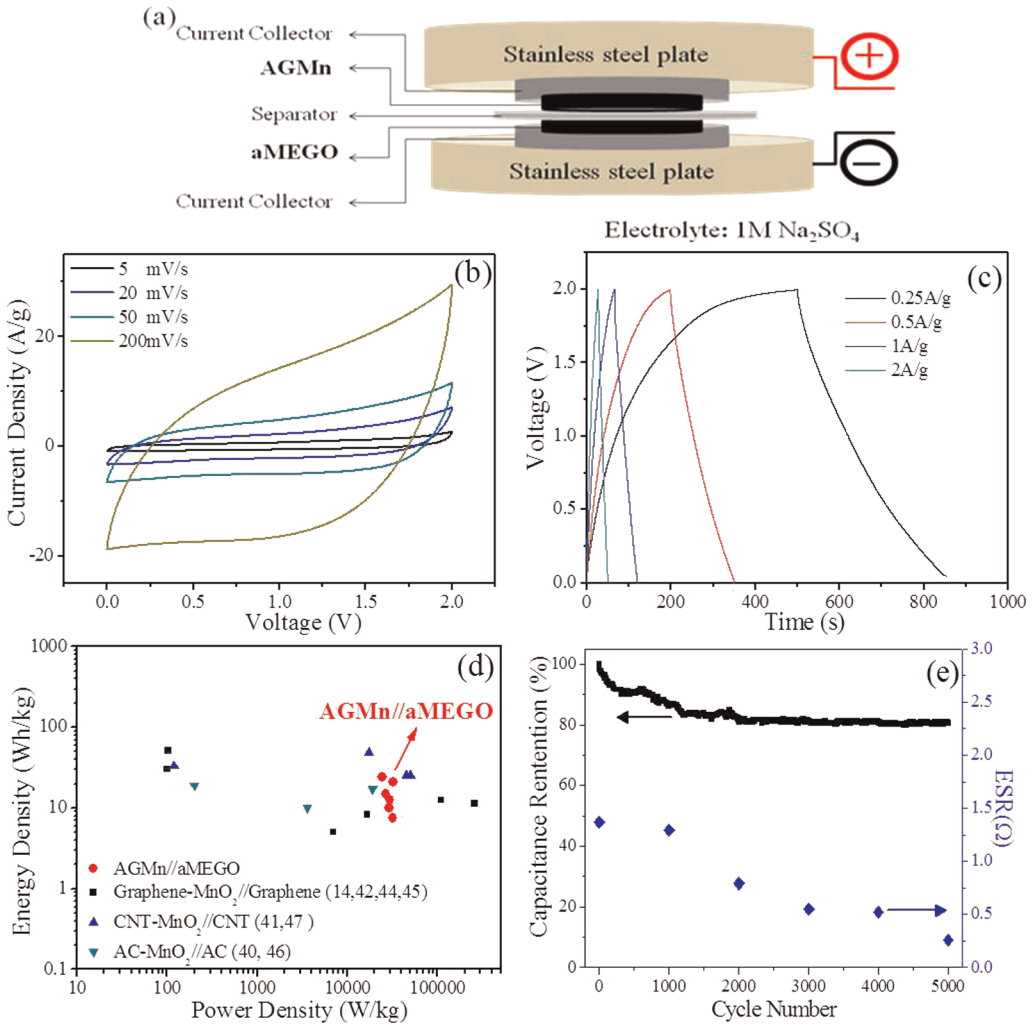

Figure 6. (a) Schematic of the assembled structure of asymmetric hybrid EC cells based on AGMn as positive electrode and aMEGO as negative electrode in aqueous electrolyte. (b) Cyclic voltammograms and (c) galvanostatic charge/discharge curves measured with different scan rates for the assembled hybrid ECs. (d) Ragone plot of energy density *versus* power density for our hybrid ECs (red points) and others using similar systems reported in the literature. (e) Cycling performance of our hybrid ECs showing capacitance retention of 80.4% after 5000 cycles of charge/discharge cycling at a current density of 2 A/g, and small change in EC's equivalent series resistance taken from impedance measurement every 1000 cycles.

carbon asymmetric system,[46] the operating voltage window in acid electrolyte was limited due to H_2 gas evolution from the reaction of H^+ ions. In a neutral electrolyte, the concentration of H^+ and OH^- ions is too low to induce gas evolution reactions, thus extending the operating voltage for asymmetric systems. For our asymmetric cells, the operating voltage with 1 M H_2SO_4 aqueous electrolyte was limited to ~1.2 V; while in Na_2SO_4 aqueous electrolyte, good capacitive behavior with rectangular CV curves at a scan rate of 20 mV/s with a potential window up to 2.0 V was obtained (Figure S6). Thus, a 1 M Na_2SO_4 aqueous solution was chosen as the electrolyte for the asymmetric systems.

Figure 6b shows the CV curves of the asymmetric ECs measured at scan rates ranging from 5 to 400 mV/s. Between 0 and 2 V, these CV curves exhibit nearly rectangular shapes without obvious redox peaks. As the scan rate is increased to 200 mV/s, the shape of CV curve shows some deviation from that of an ideal capacitor, possibly due to increasing overpotentials from ion transport between the electrolyte and MnO_2.[16] Galvanostatic charge/discharge testing was also performed with different current densities with a voltage window of 0−2 V (Figure 6c). The specific capacitance calculated on the basis of the total mass of active materials from positive and negative electrodes reached 175 F/g at a current density of 0.25 A/g. The energy (*E*) and power densities (*P*) for the asymmetric ECs were calculated from galvanostatic discharge curves and plotted on the Ragone diagram shown in Figure 6d. We also included the performance of other hybrid ECs that have been reported in the literature. The maximum energy density of 24.3 Wh/kg (at a power density of 24.5 kW/kg) and power density of 32.3 kW/kg (at a energy density of 20.8 Wh/kg) were achieved using hybrid ECs at an operating voltage of 2 V. These values are not only higher than

most of the hybrid ECs based on MnO_2/carbon electrodes[14,40,43,45,47−49] but also comparable to those of CNT-based hybrid systems.[25,41,44,50] In addition, our hybrid ECs also show good cycle life with a capacitance retention of 80.4% after 5000 charge/discharge cycles at a current density of 2 A/g. A frequency response analysis was performed after every 1000 cycles to monitor any changes in the equivalent series resistance of the cell. It demonstrates a small drop of ESR values (from 1.4 to 0.8 ohms) in the first 2000 cycles with only subtle changes for the remaining cycles.

CONCLUSION

In summary, aMEGO/MnO_2 composites were synthesized *via* a straightforward and scalable self-controlled redox process. The aMEGO with its high electrical conductivity and nanoscale pore size distribution was shown to be an excellent scaffold for MnO_2 nanoparticles. The resultant 3D AGMn composite architecture facilitates transport of both electrolyte ions and electrons to the electrode surface. The uniform size and spatial distribution of MnO_2 nanoparticles enhances the utilization of the pseudocapacitive materials, giving the composite a high specific capacitance, good rate capability, and long cycle life. We believe that such low-cost, high-performance composites using earth-abundant and environmentally friendly materials and created by a scalable solution-based process can offer great promise in grid-scale energy storage device applications.

EXPERIMENTAL SECTION

Preparation of AGMn Composites. The "activated microwave expanded graphite oxide" (aMEGO) powder was synthesized by KOH chemical activation of microwave exfoliated graphite oxide as described in our previous report.[26] The aMEGO powder was first vacuum-dried at 120 °C for about 5 h. The aMEGO/MnO_2 composites (AGMn) were then prepared using a self-controlled redox deposition process as follows: 25 mg of aMEGO powder was added to 600 mL of 0.5 mM $KMnO_4$ diluted aqueous solution while stirring in ambient at room temperature. After the reaction, the samples were filtered, washed repeatedly with deionized water, and dried in air at about 80 °C for 24 h. Different reaction durations ranging from 5 to 120 min were used to control the mass loading of MnO_2. The as-prepared samples are designated as AGMn-*x*min (x = 5, 10, 30, 60, 90, 120). The AGMn-10min and AGMn-120min samples were further calcined in air at about 400 °C for 3 h to obtain AGMn-10min-h and AGMn-120min-h. It should be pointed out that the calcinations did not change the oxidation of MnO_2 nanoparticles as the powder maintains its structural characteristics after heat treatment at temperatures lower than 400 °C for 3 h.[51,52]

General Characterization. The structure of the AGMn composites obtained was characterized by X-ray diffraction (XRD) (Xpert, Philips) using Cu Kα radiation. Transmission electron microscopy (TEM, JEOL 2010F, 200 kV) and scanning electron microscopy (SEM, Hitachi S5500, 30 kV) equipped with scanning transmission electron microscopy (STEM) and energy-dispersive spectroscopy (Bruker EDS Quantax 4010) were used to study the morphology and microstructure of the composites. An EDS mapping with specimen-drift autocompensation enabled imaging the elemental distribution with enhanced sensitivity and spatial resolution across the sample. In SEM-EDS mode, the image contrast is proportional to the mass density times the atomic number squared. Thermogravimetric analysis (TGA, Perkin-Elmer TGA 4000) was measured with a heating rate of 5 °C/min under 20 mL/min of flowing air. X-ray photoelectron spectroscopy (XPS) analysis was conducted with two separate systems equipped with monochromatic Al Kα sources (Kratos AXIS Ultra DLD, Omicron Nanotechnology XM1000/EA 125 U7) to analyze the chemical composition of the samples. The measurement of the nitrogen adsorption isotherms was done with a Quantachrome Nova 2000 at 77.4 K.

Supercapacitor Measurements. A two-electrode cell configuration was used to measure the performance of supercapacitors composed of aMEGO and AGMn composite electrodes in 1 M H_2SO_4 and 1 M Na_2SO_4 aqueous electrolytes. Polytetrafluoroethylene (5 wt %) (PTFE; 60 wt % dispersion in water) was added to the aMEGO and AGMn as a binder. Typically, the aMEGO and AGMn powders were mixed into a paste using a mortar and pestle, rolled into uniform sheets with thicknesses ranging between 40 and 50 μm, and finally punched into ∼1/4 cm diameter electrodes. A pair of typical electrodes had a weight between 0.7 and 1.4 mg after drying overnight at a ∼120 °C under vacuum. In a symmetric system, the two identical (by weight and size) aMEGO or AGMn composite electrodes were assembled in a test cell as shown in our previous report,[26] which consisted of two current collectors, two electrodes, and an ion-porous separator (Celgard 3501) supported in a test fixture consisting of two stainless steel plates. Conductive carbon-coated aluminum foils (Expoack 0.5 mil 2-side coating) were used as current collectors. The asymmetric hybrid EC cells were assembled in the same test fixture using AGMn composites for the positive electrodes and aMEGO for the negative electrodes. For the asymmetric cells, the electrodes were ∼1/4 cm in diameter with thicknesses of ∼40−50 μm.

The total gravimetric specific capacitances were calculated from the constant current charge/discharge curves using the following equation: $C = 4I\Delta t/(m\Delta V)$, where I (A) is the discharge current, Δt (s) is the discharge time, m (g) is the mass of the two identical electrodes, and ΔV (V) is the voltage range of the discharge portion. Equivalent series resistance (ESR) was estimated using the voltage drop at the beginning of the discharge, V_{drop} (V), at certain constant current I (A), with the formula $R_{ESR} = V_{drop}/(2I)$. The energy density was estimated by using the formula $E = CV_{max}^2/8$. The power density, calculated from the constant current discharge curves and normalized with the total weight of two electrodes m (g), is given by $P = (V_{max} - V_{drop})^2/(4R_{ESR}m)$.

Conflict of Interest: The authors declare no competing financial interest.

Acknowledgment. We appreciate funding support from the U.S. Department of Energy (DOE) under award DE-SC0001951 and the Institute of Advanced Technology. Y.Z. thanks the support from National Basic Research Program of China with award No. 2012CB922001. X.Z. and Q.H.Z. are supported by the China Scholarship Council Fellowship.

Supporting Information Available: TGA analysis data, XPS, SEM images, TEM images, and electrochemical performance for typical samples. This material is available free of charge *via* the Internet at http://pubs.acs.org.

REFERENCES AND NOTES

1. Simon, P.; Gogotsi, Y. Materials for Electrochemical Capacitors. *Nat. Mater.* **2008**, *7*, 845–854.
2. Zhang, L. L.; Zhao, X. S. Carbon-Based Materials as Supercapacitor Electrodes. *Chem. Soc. Rev.* **2009**, *38*, 2520–2531.
3. Chmiola, J.; Yushin, G.; Gogotsi, Y.; Portet, C.; Simon, P.; Taberna, P. L. Anomalous Increase in Carbon Capacitance

at Pore Sizes Less Than 1 Nanometer. *Science* **2006**, *313*, 1760–1763.
4. Frackowiak, E.; Beguin, F. Carbon Materials for the Electrochemical Storage of Energy in Capacitors. *Carbon* **2001**, *39*, 937–950.
5. Hu, C. C.; Chang, K. H.; Lin, M. C.; Wu, Y. T. Design and Tailoring of the Nanotubular Arrayed Architecture of Hydrous RuO_2 for Next Generation Supercapacitors. *Nano Lett.* **2006**, *6*, 2690–2695.
6. Du, X. A.; Wang, C. Y.; Chen, M. M.; Jiao, Y. Electrochemical Properties of Hybrid Supercapacitor with Nanosized Fe_3O_4/Activated Carbon as Electrodes. *J. Inorg. Mater.* **2008**, *23*, 1193–1198.
7. Yuan, C. Z.; Zhang, X. G.; Su, L. H.; Gao, B.; Shen, L. F. Facile Synthesis and Self-Assembly of Hierarchical Porous NiO Nano/Micro Spherical Superstructures for High Performance Supercapacitors. *J. Mater. Chem.* **2009**, *19*, 5772–5777.
8. Nam, K. W.; Kim, K. B. A Study of the Preparation of NiO_x Electrode *via* Electrochemical Route for Supercapacitor Applications and Their Charge Storage Mechanism. *J. Electrochem. Soc.* **2002**, *149*, A346–A354.
9. Prasad, K. R.; Miura, N. Electrochemically Synthesized MnO_2-Based Mixed Oxides for High Performance Redox Supercapacitors. *Electrochem. Commun.* **2004**, *6*, 1004–1008.
10. Li, Y. Z.; Zhao, X.; Xu, Q.; Zhang, Q. H.; Chen, D. J. Facile Preparation and Enhanced Capacitance of the Polyaniline/Sodium Alginate Nanofiber Network for Supercapacitors. *Langmuir* **2011**, *27*, 6458–6463.
11. Fan, L. Z.; Maier, J. High-Performance Polypyrrole Electrode Materials for Redox Supercapacitors. *Electrochem. Commun.* **2006**, *8*, 937–940.
12. Stenger-Smith, J. D.; Webber, C. K.; Anderson, N.; Chafin, A. P.; Zong, K. K.; Reynolds, J. R. Poly(3,4-alkylenedioxythiophene)-Based Supercapacitors Using Ionic Liquids as Supporting Electrolytes. *J. Electrochem. Soc.* **2002**, *149*, A973–A977.
13. Frackowiak, E.; Khomenko, V.; Jurewicz, K.; Lota, K.; Beguin, F. Supercapacitors Based on Conducting Polymers/Nanotubes Composites. *J. Power Sources* **2006**, *153*, 413–418.
14. Yu, G. H.; Hu, L. B.; Vosgueritchian, M.; Wang, H. L.; Xie, X.; McDonough, J. R.; Cui, X.; Cui, Y.; Bao, Z. N. Solution-Processed Graphene/MnO_2 Nanostructured Textiles for High-Performance Electrochemical Capacitors. *Nano Lett.* **2011**, *11*, 2905–2911.
15. Toupin, M.; Brousse, T.; Belanger, D. Charge Storage Mechanism of MnO_2 Electrode Used in Aqueous Electrochemical Capacitor. *Chem. Mater.* **2004**, *16*, 3184–3190.
16. Ivey, D. G.; Wei, W. F.; Cui, X. W.; Chen, W. X. Manganese Oxide-Based Materials as Electrochemical Supercapacitor Electrodes. *Chem. Soc. Rev.* **2011**, *40*, 1697–1721.
17. He, S. Y.; Peng, Y. T.; Chen, Z.; Wen, J.; Xiao, Q. F.; Weng, D.; Geng, H. B.; Lu, Y. F. Hierarchical Manganese Oxide/Carbon Nanocomposites for Supercapacitor Electrodes. *Nano Res.* **2011**, *4*, 216–225.
18. Li, W. C.; Wang, Y. T.; Lu, A. H.; Zhang, H. L. Synthesis of Nanostructured Mesoporous Manganese Oxides with Three-Dimensional Frameworks and Their Application in Supercapacitors. *J. Phys. Chem. C* **2011**, *115*, 5413–5421.
19. McEvoy, T. M.; Long, J. W.; Smith, T. J.; Stevenson, K. J. Nanoscale Conductivity Mapping of Hybrid Nanoarchitectures: Ultrathin Poly(*o*-phenylenediamine) on Mesoporous Manganese Oxide Ambigels. *Langmuir* **2006**, *22*, 4462–4466.
20. Nagarajan, N.; Humadi, H.; Zhitomirsky, I. Cathodic Electrodeposition of MnO_x Films for Electrochemical Supercapacitors. *Electrochim. Acta* **2006**, *51*, 3039–3045.
21. Nam, K. W.; Kim, K. B. Manganese Oxide Film Electrodes Prepared by Electrostatic Spray Deposition for Electrochemical Capacitors. *J. Electrochem. Soc.* **2006**, *153*, A81–A88.
22. Dong, X. P.; Shen, W. H.; Gu, J. L.; Xiong, L. M.; Zhu, Y. F.; Li, Z.; Shi, J. L. MnO_2-Embedded-in-Mesoporous-Carbon-Wall Structure for Use as Electrochemical Capacitors. *J. Phys. Chem. B* **2006**, *110*, 6015–6019.
23. Fuertes, A. B.; Alvarez, S. Graphitic Mesoporous Carbons Synthesised through Mesostructured Silica Templates. *Carbon* **2004**, *42*, 3049–3055.
24. Choi G. B.; Yang, M.; Hong, W. H.; Choi, J. W.; Huh Y. S. 3D Macroporous Graphene Frameworks for Supercapacitors with High Energy and Power Densities. *ACS Nano* **2012**, DOI: 10.1021/nn3003345.
25. Kim, J. H.; Lee, K. H.; Overzet, L. J.; Lee, G. S. Synthesis and Electrochemical Properties of Spin-Capable Carbon Nanotube Sheet/MnO_x Composites for High-Performance Energy Storage Devices. *Nano Lett.* **2011**, *11*, 2611–2617.
26. Zhu, Y. W.; Murali, S.; Stoller, M. D.; Ganesh, K. J.; Cai, W. W.; Ferreira, P. J.; Pirkle, A.; Wallace, R. M.; Cychosz, K. A.; Thommes, M.; *et al.* Carbon-Based Supercapacitors Produced by Activation of Graphene. *Science* **2011**, *332*, 1537–1541.
27. Jin, X.; Zhou, W.; Zhang, S.; Chen, G. Z. Nanoscale Microelectrochemical Cells on Carbon Nanotubes. *Small* **2007**, *3*, 1513–1517.
28. Zhang, L. L.; Wei, T. X.; Wang, W. J.; Zhao, X. S. Manganese Oxide-Carbon Composite as Supercapacitor Electrode Materials. *Microporous Mesoporous Mater.* **2009**, *123*, 260–267.
29. Kim, T. W.; Park, I. S.; Ryoo, R. A Synthetic Route to Ordered Mesoporous Carbon Materials with Graphitic Pore Walls. *Angew. Chem., Int. Ed.* **2003**, *42*, 4375–4379.
30. Tan, B. J.; Klabunde, K. J.; Sherwood, P. M. A. XPS Studies of Solvated Metal Atom Dispersed Catalystes Evidence for Layered Cobalt-Manganese Particles on Alumina and Silica. *J. Am. Chem. Soc.* **1991**, *113*, 855–861.
31. Patel, M. N.; Wang, X. Q.; Wilson, B.; Ferrer, D. A.; Dai, S.; Stevenson, K. J.; Johnston, K. P. Hybrid MnO_2-Disordered Mesoporous Carbon Nanocomposites: Synthesis and Characterization as Electrochemical Pseudocapacitor Electrodes. *J. Mater. Chem.* **2010**, *20*, 390–398.
32. Zhu, S. M.; Zhou, H. A.; Hibino, M.; Honma, I.; Ichihara, M. Synthesis of MnO_2 Nanoparticles Confined in Ordered Mesoporous Carbon Using a Sonochemical Method. *Adv. Funct. Mater.* **2005**, *15*, 381–386.
33. Fischer, A. E.; Pettigrew, K. A.; Rolison, D. R.; Stroud, R. M.; Long, J. W. Incorporation of Homogeneous, Nanoscale MnO_2 within Ultraporous Carbon Structures *via* Self-Limiting Electroless Deposition: Implications for Electrochemical Capacitors. *Nano Lett.* **2007**, *7*, 281–286.
34. Zhang, W. H.; Shi, J. L.; Chen, H. R.; Hua, Z. L.; Yan, D. S. Synthesis and Characterization of Nanosized ZnS Confined in Ordered Mesoporous Silica. *Chem. Mater.* **2001**, *13*, 648–654.
35. Zhang, L. X.; Shi, J. L.; Yu, J.; Hua, Z. L.; Zhao, X. G.; Ruan, M. L. A New *In-Situ* Reduction Route for the Synthesis of Pt Nanoclusters in the Channels of Mesoporous Silica SBA-15. *Adv. Mater.* **2002**, *14*, 1510–1513.
36. Li, L.; Shi, J. L.; Zhang, L. X.; Xiong, L. M.; Yan, J. N. A Novel and Simple *In-Situ* Reduction Route for the Synthesis of an Ultra-thin Metal Nanocoating in the Channels of Mesoporous Silica Materials. *Adv. Mater.* **2004**, *16*, 1079–1082.
37. Li, Z. P.; Wang, J. Q.; Liu, S.; Liu, X. H.; Yang, S. R. Synthesis of Hydrothermally Reduced Graphene/MnO_2 Composites and Their Electrochemical Properties as Supercapacitors. *J. Power Sources* **2011**, *196*, 8160–8165.
38. Zhang, H.; Cao, G. P.; Wang, Z. Y.; Yang, Y. S.; Shi, Z. J.; Gu, Z. N. Growth of Manganese Oxide Nanoflowers on Vertically-Aligned Carbon Nanotube Arrays for High-Rate Electrochemical Capacitive Energy Storage. *Nano Lett.* **2008**, *8*, 2664–2668.
39. Chen, L.; Sun, L. J.; Luan, F.; Liang, Y.; Li, Y.; Liu, X. X. Synthesis and Pseudocapacitive Studies of Composite Films of Polyaniline and Manganese Oxide Nanoparticles. *J. Power Sources* **2010**, *195*, 3742–3747.
40. Hou, Y.; Cheng, Y. W.; Hobson, T.; Liu, J. Design and Synthesis of Hierarchical MnO_2 Nanospheres/Carbon Nanotubes/Conducting Polymer Ternary Composite for High Performance Electrochemical Electrodes. *Nano Lett.* **2010**, *10*, 2727–2733.

41. Zhou, Y. K.; He, B. L.; Zhang, F. B.; Li, H. L. Hydrous Manganese Oxide/Carbon Nanotube Composite Electrodes for Electrochemical Capacitors. *J. Solid State Electrochem.* **2004**, *8*, 482–487.
42. Lang, X. Y.; Hirata, A.; Fujita, T.; Chen, M. W. Nanoporous Metal/Oxide Hybrid Electrodes for Electrochemical Supercapacitors. *Nat. Nanotechnol.* **2011**, *6*, 232–236.
43. Cottineau, T.; Toupin, M.; Delahaye, T.; Brousse, T.; Belanger, D. Nanostructured Transition Metal Oxides for Aqueous Hybrid Electrochemical Supercapacitors. *Appl. Phys. A: Mater. Sci. Process.* **2006**, *82*, 599–606.
44. Chen, P. C.; Shen, G.; Shi, Y.; Chen, H.; Zhou, C. Preparation and Characterization of Flexible Asymmetric Supercapacitors Based on Transition-Metal-Oxide Nanowire/Single-Walled Carbon Nanotube Hybrid Thin-Film Electrodes. *ACS Nano* **2010**, *4*, 4403–4411.
45. Fan, Z. J.; Yan, J.; Wei, T.; Zhi, L. J.; Ning, G. Q.; Li, T. Y.; Wei, F. Asymmetric Supercapacitors Based on Graphene/MnO_2 and Activated Carbon Nanofiber Electrodes with High Power and Energy Density. *Adv. Funct. Mater.* **2011**, *21*, 2366–2375.
46. Hong, M. S.; Lee, S. H.; Kim, S. W. Use of KCl Aqueous Electrolyte for 2 V Manganese Oxide/Activated Carbon Hybrid Capacitor. *Electrochem. Solid State Lett.* **2002**, *5*, A227–A230.
47. Wu, Z. S.; Ren, W. C.; Wang, D. W.; Li, F.; Liu, B. L.; Cheng, H. M. High-Energy MnO_2 Nanowire/Graphene and Graphene Asymmetric Electrochemical Capacitors. *ACS Nano* **2010**, *4*, 5835–5842.
48. Cheng, Q.; Tang, J.; Ma, J.; Zhang, H.; Shinya, N.; Qin, L. C. Graphene and Nanostructured MnO_2 Composite Electrodes for Supercapacitors. *Carbon* **2011**, *49*, 2917–2925.
49. Brousse, T.; Toupin, M.; Belanger, D. A Hybrid Activated Carbon-Manganese Dioxide Capacitor Using a Mild Aqueous Electrolyte. *J. Electrochem. Soc.* **2004**, *151*, A614–A622.
50. Yan, J.; Fan, Z. J.; Wei, T.; Cheng, J.; Shao, B.; Wang, K.; Song, L. P.; Zhang, M. L. Carbon Nanotube/MnO_2 Composites Synthesized by Microwave-Assisted Method for Supercapacitors with High Power and Energy Densities. *J. Power Sources* **2009**, *194*, 1202–1207.
51. Ragupathy, P.; Park, D. H.; Campet, G.; Vasan, H. N.; Hwang, S. J.; Choy, J. H.; Munichandraiah, N. Remarkable Capacity Retention of Nanostructured Manganese Oxide Upon Cycling as an Electrode Material for Supercapacitor. *J. Phys. Chem. C* **2009**, *113*, 6303–6309.
52. Ragupathy, P.; Vasan, H. N.; Munichandraiah, N. Synthesis and Characterization of Nano-MnO_2 for Electrochemical Supercapacitor Studies. *J. Electrochem. Soc.* **2008**, *155*, A34–A40.